

Modeling damage in polymeric composites

N.M. Hassan, R.C. Batra *

Department of Engineering Science and Mechanics, MIC 0219, Virginia Polytechnic Institute and State University, Blacksburg, VA 24061, United States

Available online 16 February 2007

Abstract

We postulate that dominant damage modes in a fiber-reinforced laminated composite are fiber breakage, matrix cracking, fiber/matrix debonding, and delamination/sliding. The first three damage modes are represented by internal variables with their development governed by constitutive relations. The delamination/sliding failure mode is presumed to initiate at a point on an interface between two adjoining layers when the transverse shear and the transverse normal stresses there are on a failure surface defined in the stress space. Equations expressing the balance of mass, the balance of linear momentum, the balance of moment of momentum, material response, and those giving the development of damage are simultaneously solved numerically under prescribed initial and boundary conditions to find an approximate solution of a transient 3-dimensional initial-boundary-value (IBV) problem. Values of material parameters for the AS4/PEEK composite are determined from experimental data available in the literature. The developed mathematical model has been validated by comparing computed results, for several IBV problems different from the ones used to find values of material parameters, with the corresponding experimental results available in the literature.

© 2007 Elsevier Ltd. All rights reserved.

Keywords: A. Polymer–matrix composites; C. Damage mechanics; C. Finite element analysis; Transient 3-dimensional deformations

1. Introduction

Damage in composites, which often is undetectable, includes matrix cracks, fiber breakage, fiber/matrix debonding, and delamination/sliding of two adjoining layers. Even when the damage does not cause catastrophic failure, it significantly reduces structural stiffness. Many researchers, for example VinÇon et al. [1], Vogler and Kyriakides [2], Stout et al. [3], Gilbert et al. [4], Steeves and Fleck [5], have experimentally studied the failure of polymeric composites. Other investigators, e.g. Matzenmiller et al. [6], Zhu and Cescotto [7], Voyiadjis and Deliktas [8], Zhu and Sun [9], Espinosa et al. [10], Williams and Vaziri [11], Tang et al. [12], Maa and Cheng [13], have employed numerical and analytical methods to predict damage initiation and propagation in composite structures. It is common to assume that damage initiates at a point when the state of deformation and/or stress there lies on a damage envelope defined in terms of the equivalent stress, or the

equivalent strain, or their combination. The moduli are assumed to degrade with the development of damage till they become zero, and the material point then is taken to have failed completely. Other criteria for predicting damage include a fracture mechanics approach based on the energy release rate, or a distributed damage mechanics approach involving an evolution equation for damage that must be integrated together with equations of motion.

Continuum Damage Mechanics (CDM), initiated by Kachanov [14], and Rabotnov [15], assumes that a micro-mechanical process can be treated at a macro-level by homogenizing the damage over a Representative Volume Element (RVE) since the damage manifests itself as a distribution of voids in the material. Coleman and Noll [16] developed a thermodynamic theory of materials with internal variables; an internal variable is non-observable, is obtained from an evolution law, and may be associated with a damage variable. Talreja [17] identified damage with the gradual deterioration of a material due to the initiation and growth of micro-cracks and micro-voids. Ladveze [18] followed a similar approach, and used CDM to describe the deterioration of a material's strength. In addition, an

* Corresponding author. Tel.: +1 540 231 6051; fax: +1 540 231 4574.
E-mail address: rbatra@vt.edu (R.C. Batra).

elasto-plastic material behavior with no coupling between the damage and the plastic deformations was assumed with elastic deformations obeying Hooke's law. Zhu and Cescotto [7] developed a CDM theory for anisotropic elastoviscoplastic materials undergoing finite strains, and studied their ductile fracture. Matzenmiller et al. [6] proposed, for a lamina, a CDM based model with three damage parameters; two associated with the in-plane principal lamina directions, and the third representing the effect of damage in shear. Barberis et al. [19] implemented CDM in an existing finite element (FE) code to predict progressive damage growth in laminated composites. The damage, represented by two scalar variables, was introduced in the constitutive equation of the material to express the reduction in stiffness. Voyiadjis and Deliktas [8] developed a coupled incremental damage and plasticity theory for rate-independent composites with von Mises yield criterion and the associated flow rule to describe plastic deformations.

Zhu and Sun [9] described the rate-dependent behavior of a polymeric composite during loading and unloading with a three parameter overstress viscoplastic constitutive relation. A multi-step relaxation procedure was used to establish the equilibrium stress for both loading and unloading. The model was used to predict the rate-dependent loading, and unloading behavior of the IM7/5260 composite. A three-dimensional (3-D) finite deformation anisotropic viscoplasticity model for fiber-reinforced composites in total Lagrangian description of motion was proposed by Espinosa et al. [10]. Nine coefficients in the plastic potential, given by a quadratic function of the second Piola–Kirchhoff stress tensor, were reduced to two by assuming that the axially loaded fibers deform linear elastically up to failure, and fiber volume fractions in two principal directions are equal to each other. Values of these constants were experimentally determined through off-axis tension, and out of plane shear tests. A power law rule was used to account for the effect of strain rate and temperature by defining the material strength in terms of an effective stress that includes temperature, and strain rate terms. They also conducted tests to determine parameters in the viscoplastic relation, and found that it could not adequately describe composite's response after first failure.

First [20], second [21–26], and fourth-order [27–29] damage tensors have been proposed to account for the anisotropy of damage; even eighth order damage tensors were proposed to account for the effect of crack shape, and orientation [11]. Tang et al. [12] derived constitutive equations for a damaged anisotropic elastic material undergoing infinitesimal isothermal deformations with damage functions determined from micro-mechanics principles. An example was given for the problem of distributed needle-shaped micro-voids, and the solution of the micro-mechanical problem was obtained by employing the Eshelby–Mori–Tanaka scheme. However, effects of micro-crack closure, and coupling of damage with plastic deformations were not considered. Maa and Cheng [13] developed a CDM failure model for predicting the strength of notched composite

laminates. They considered damage due to fiber breakage, matrix cracking, and fiber/matrix debonding, and adopted associative flow rules, i.e., the damage, and the yield surfaces were taken to coincide with the corresponding potential surfaces. The material was assumed to be linear elastic, and two terms were added to the free energy function to describe the effect of accumulated matrix damage and accumulated plastic shear strain. This model was used to predict the ultimate failure load of a laminate containing a circular hole.

The failure mechanisms, and processes on a micro-mechanical scale vary with the type of loading, and are intimately related to properties of its constituents, i.e. matrix, fiber, and interface. Micro-level failure mechanisms include fiber fracture, fiber buckling, fiber splitting, fiber pullout, fiber/matrix debonding, and matrix cracking. Accurate modeling of these failure mechanisms requires too many internal variables, the identification of an internal variable with a failure mode is tedious, and the determination of material parameters from test data very arduous. Here, a CDM approach with three scalar internal variables, ϕ^f , ϕ^m , and ϕ^d , denoting, respectively, the damage accumulation in fiber (fiber fracture, fiber buckling, fiber pullout), matrix cracking, and fiber/matrix debonding is used. The scalar variables are related to the overall composite constituent properties using a Mechanics of Materials (MoM) approach. The capacity of a material point to support any load vanishes when all three damage variables equal 1.0 there. Values of material parameters are determined for the AS4/PEEK composite by using test data available in the literature. The delamination/sliding between adjoining layers is simulated by postulating a damage surface in terms of transverse normal, and transverse shear stresses acting on an interface. When the stress state at a point of the interface lies on this surface, delamination is assumed to ensue from that point. Different case studies are simulated to predict qualitatively, and quantitatively the failure modes. Computed numerical results are found to compare well with experimental findings available in the literature. The objective is to develop, and validate a simple mathematical model, having few variables, for analyzing deformations of a composite that can predict reasonably well different failure modes.

2. Problem formulation

2.1. Balance laws

In the referential description of motion, the balance of mass, the balance of linear momentum, the balance of moment of momentum, and the balance of internal energy are

$$\rho(\mathbf{X}, t)J(\mathbf{X}, t) = \rho_R(\mathbf{X}), \quad (1)$$

$$\rho_R \dot{v}_i = T_{i\alpha,\alpha} + \rho_R b_i, \quad (2)$$

$$\mathbf{T}\mathbf{F}^T = (\mathbf{T}\mathbf{F}^T)^T, \quad (3)$$

$$\rho_R \dot{e} = -\tilde{Q}_{\alpha,\alpha} + T_{i\alpha} \dot{F}_{i\alpha} + \rho_R s, \quad (4)$$

where ρ is the mass density of the material particle X at time t , ρ_R its mass density in the reference configuration, \mathbf{F} the deformation gradient, $J = \det F_{ix} \neq 0$ the determinant of the deformation gradient, \mathbf{T} the first Piola–Kirchhoff stress tensor, $T_{ix,\beta} \equiv \partial T_{ix} / \partial X_\beta$, \mathbf{b} the body force per unit mass, a superimposed dot indicates the material time derivative, e is the specific internal energy, \mathbf{Q} the heat flux per unit area in the reference configuration, and s the specific supply of internal energy. Eqs. (1)–(4) are to be supplemented by constitutive relations, initial conditions, and boundary conditions. We assume that the constitutive relation for \mathbf{T} identically satisfies the balance of moment of momentum (3).

2.2. Constitutive relations

We use the theory of internal variables to describe damage evolution in rate and temperature dependent bodies. Let

$$\xi = \{\phi^m, \phi^f, \phi^d\}, \quad (5)$$

be the ordered set of internal variables, and

$$\omega = \{Y^m, Y^f, Y^d\}, \quad (6)$$

be the ordered set of corresponding conjugate forces. We follow Coleman and Noll's [16] approach for deriving constitutive relations from the second law of thermodynamics or an entropy inequality, and assume that constitutive relations are such that when they are substituted into balance laws, and the resulting field equations solved for the position \mathbf{x} , and the absolute temperature θ , \mathbf{x} and θ satisfy the Clausius–Duhem inequality. We postulate that ψ , \mathbf{S} , \mathbf{Q} , η and e are functions of $\mathbf{E} = (\mathbf{F}^T \mathbf{F} - \mathbf{I})/2$, $\dot{\mathbf{E}}$, θ , $\mathbf{G} = \text{Grad } \theta$, and ξ , follow the usual procedure (e.g. see [16]), assume that ξ does not depend upon θ , $\dot{\mathbf{E}}$ and \mathbf{G} , and get

$$\frac{\partial \psi}{\partial \mathbf{G}_\alpha} = 0, \quad \eta = -\frac{\partial \psi}{\partial \theta}, \quad \frac{\partial \psi}{\partial \dot{\mathbf{E}}_{\alpha\beta}} = 0, \quad (7)$$

where $\psi = e - \theta\eta$, denotes the specific Helmholtz free energy, \mathbf{S} the second Piola–Kirchhoff stress tensor, and η the specific entropy.

Let

$$\mathbf{S}(\mathbf{E}, \dot{\mathbf{E}}, \theta, \mathbf{G}, \xi) = \mathbf{S}^e(\mathbf{E}, \theta, \theta, \theta, \xi) + \mathbf{S}^{nc}(\mathbf{E}, \dot{\mathbf{E}}, \theta, \mathbf{G}, \xi), \quad (8)$$

$$S_{\alpha\beta}^e(\mathbf{E}, \theta, \theta, \theta, \xi) \equiv \rho_R \frac{\partial \psi}{\partial E_{\alpha\beta}},$$

and

$$\omega(\mathbf{E}, \dot{\mathbf{E}}, \theta, \mathbf{G}, \xi) = \omega^e(\mathbf{E}, \theta, \theta, \theta, \xi) + \omega^{nc}(\mathbf{E}, \dot{\mathbf{E}}, \theta, \mathbf{G}, \xi),$$

$$\omega^e(\mathbf{E}, \theta, \theta, \theta, \xi) \equiv -\rho_R \frac{\partial \psi}{\partial \xi}, \quad (9)$$

where \mathbf{S}^e (equilibrium stress) denotes the value of the stress tensor \mathbf{S} at zero strain rate and zero temperature gradient, and ω^e the value of the thermodynamic force ω at zero

strain rate and zero temperature gradient. The tensor \mathbf{I} is the identity tensor, \mathbf{E} the Green–St. Venant tensor, and in terms of the displacement vector \mathbf{u} ,

$$E_{\alpha\beta} = \frac{1}{2} \left(\frac{\partial u_\alpha}{\partial X_\beta} + \frac{\partial u_\beta}{\partial X_\alpha} + \frac{\partial u_i}{\partial X_\alpha} \frac{\partial u_i}{\partial X_\beta} \right). \quad (10)$$

Substitution from Eqs. (7)–(9) into the Clausius–Duhem inequality gives the following dissipation inequality:

$$D_{\text{en}} \equiv S_{\alpha\beta}^{nc} \dot{E}_{\alpha\beta} + \sum_i \omega_{(i)}^e \dot{\xi}^{(i)} - \frac{\tilde{\mathbf{Q}}_\alpha \mathbf{G}_\alpha}{\theta} \geq 0. \quad (11)$$

Here, D_{en} is the rate of energy dissipated per unit volume in the reference configuration. It is evident that D_{en} is minimum when $\dot{E}_{\alpha\beta} = 0$, $\dot{\xi} = 0$, and $\mathbf{G} = \mathbf{0}$. Therefore,

$$\tilde{\mathbf{Q}}|_e = 0, \quad K_{\alpha\beta} = -\frac{\partial \tilde{\mathbf{Q}}_\alpha}{\partial \mathbf{G}_\beta}|_e \geq 0, \quad (12)$$

where $f|_e$ indicates the value of f when $\dot{\mathbf{E}} = \mathbf{0}$, $\dot{\xi} = \mathbf{0}$, and $\mathbf{G} = \mathbf{0}$, usually called an equilibrium state. That is, the heat flux vanishes in the absence of temperature gradient, and the thermal conductivity tensor, \mathbf{K} , is positive semi-definite.

Henceforth we only consider isothermal processes; therefore, we do not consider the energy equation.

Let $W = \rho_R \psi$ and

$$W = C_{\alpha\beta}^0 E_{\alpha\beta} + \frac{1}{2} C_{\alpha\beta\gamma\delta} E_{\alpha\beta} E_{\gamma\delta}, \quad (13)$$

where $C_{\alpha\beta}^0 = C_{\beta\alpha}^0$, $C_{\alpha\beta\gamma\delta} = C_{\gamma\delta\alpha\beta} = C_{\beta\alpha\gamma\delta}$, and C^0 and C are functions of ξ . Eq. (13) provides a reasonable estimate of the strain energy density W for composites since they fail at rather small strains. The tensor C^0 equals the stress in the reference configuration, and C 's are elastic moduli of the damaged material. Because of the indicated symmetries, there are 21 independent elastic moduli C . Substitutions from Eq. (13) into Eqs. (8) and (9) gives

$$S_{\alpha\beta}^e = C_{\alpha\beta}^0 + C_{\alpha\beta\gamma\delta} E_{\gamma\delta},$$

$$\omega_{(i)}^e = Y^{e(i)} = \left(-\frac{\partial C_{\alpha\beta}^0}{\partial \phi^{(i)}} E_{\alpha\beta} - \frac{1}{2} \frac{\partial C_{\alpha\beta\gamma\delta}}{\partial \phi^{(i)}} E_{\alpha\beta} E_{\gamma\delta} \right), \quad i = m, f, d. \quad (14)$$

Eq. (14)₁ accounts for geometric nonlinearities; a material described by it is usually called neo-Hookean. Batra [30] has compared the response of an isotropic neo-Hookean material with that of three other materials described by constitutive relations that relate linearly a stress tensor to a finite strain tensor. Values of elastic constants for a neo-Hookean material are the same as those for a Hookean material. Thus when deducing them from the experimental data we assume that the composite material can be modeled as Hookean. Henceforth we assume that the body is initially stress free; i.e., $C_{\alpha\beta}^0 = 0$.

2.2.1. Constitutive relations for a unidirectional lamina

We assume that a lamina reinforced with unidirectional fibers can be modeled as transversely isotropic with the axis

of transverse isotropy perpendicular to the plane of the lamina. We use rectangular Cartesian coordinates to describe lamina's deformations, and choose X_1 -axis aligned with fibers, and X_2 - and X_3 -axes perpendicular to fibers; these are usually referred to as the material principal directions. Thus there are five independent elastic constants out of the 81 components of $C_{\alpha\beta\gamma\delta}$. Components of matrix $[C]$ in terms of the more familiar elastic constants are given in Refs. [31–35,45].

The matrix of elastic constants, the second Piola–Kirchhoff stress tensor, and the Green–St. Venant strain tensor are transformed from the material principal directions to global coordinate axes and vice-a-versa by using tensor transformation rules; e.g., see [34,45].

2.2.2. Dependence of material parameters upon damage variables

We employ the MoM approach to derive the dependence of material parameters upon damage variables. As mentioned above, values of material parameters for a neo-Hookean and a Hookean material are the same, and a constitutive relation for the former is obtained from that of the latter when the infinitesimal strain tensor, $\varepsilon_{ij} = \frac{1}{2} \left(\frac{\partial u_i}{\partial x_j} + \frac{\partial u_j}{\partial x_i} \right) \delta_{ix} \delta_{j\beta}$, in Hooke's law is replaced by the finite strain tensor, \mathbf{E} . Thus without any loss of generality, for finding values of material parameters from the test data, we consider only infinitesimal strains. For infinitesimal deformations, the three stress tensors namely, the first and the second Piola–Kirchhoff stress tensors \mathbf{T} and \mathbf{S} , and the Cauchy stress tensor $\boldsymbol{\sigma}$ are equal.

The RVE composed of a single fiber embedded in a matrix is used to find the dependence of material parameters of a lamina upon the three scalar damage variables ϕ^f , ϕ^m , ϕ^d by using the MoM approach. The failure behavior under simple loading conditions observed experimentally is first reviewed, and is then used to find the dependence of material parameters upon the damage variables. For simplicity, the rectangular Cartesian coordinate axes are assumed to be aligned with the material principal directions.

The axial strength of a unidirectional lamina with fibers aligned along the loading direction is typically controlled by fiber's ultimate strain/stress. Under longitudinal tension, the phase with lower ultimate strain will fail first [32]. Agarwal and Broutman [35] have stated that in a unidirectional composite subjected to increasing longitudinal tensile load, failure initiates by fiber breakage at the weakest cross-section, and additional fibers break subsequently. Under longitudinal compression, failure is usually associated with micro-buckling or kinking of fibers within the matrix. Failure of unidirectional composites loaded in the fiber direction may be initiated by transverse splitting/debonding because the transverse tensile strain resulting from Poisson's effect can exceed the ultimate strain of the composite [32].

Under longitudinal loading, we assume that fibers carry most of the load, failure is determined by the breakage of

fibers in tension or their micro-buckling in compression, and fiber breakage can be represented by reduction in the load carrying cross-sectional area of the fiber (i.e. cross-sectional area perpendicular to the direction of the applied load) at the failure point. An RVE having a broken fiber is evinced in Fig. 1a, the effective area of fibers in the X_2X_3 -plane equals $(1 - A^{bf})$, where the area of broken fibers, A^{bf} , is given by $A^{bf} = \phi^f A^f$, A^f is the total cross-sectional area of all fibers, $\phi^f = 0$ for undamaged fibers, and $\phi^f = 1$ for totally damaged fibers. We assume strain compatibility between the two phases; it is often referred to as the Voigt model or the isostrain analysis. That is, $\varepsilon_{11}^c = \varepsilon_{11}^m = \varepsilon_{11}^f$, where superscripts c, m and f on a quantity signify its value for the composite, the matrix, and the fiber respectively. It is equivalent to assuming that all points on the two end faces of the RVE move axially by the same amount. The axial stress in the composite material is given by a weighted sum of the axial stress in each phase, and using Hooke's law, we get

$$E_1^c = E_1^f V^f (1 - \phi^f) + E_1^m V^m, \quad (15)$$

where E_1 is Young's modulus in the axial (or the fiber) direction. Following the MoM approach, see e.g. Herakovich [33], we conclude that the effective axial Poisson's ratio, ν_{13}^c , is independent of the damage induced in the fiber and the matrix, and follows the rule of mixtures. Similarly, ν_{12}^c is also given by the rule of mixtures, and is independent of the damage induced in the fiber, and the matrix.

The transverse tensile loading of a unidirectional composite causes high stress and strain concentrations in the matrix, and at the matrix/fiber interface. As for longitudinal tensile loading, failure ensues as isolated interfacial micro-cracks that increase in number, and finally coalesce into a catastrophic micro-crack [32] with minimal fiber breakage. Under transverse compression, a unidirectional composite may fail due to compressive failure in the matrix, and/or fiber crushing [32].

Matrix cracking is represented by reduction in the cross-sectional area of the matrix perpendicular to the applied load; e.g., see Fig. 1b. The effective area of the matrix in the X_1X_2 -plane/ X_1X_3 -plane is assumed to equal $(1 - A^{bm})$, where area of the cracked matrix, A^{bm} , is given by $A^{bm} = \phi^m A^m$, A^m is the cross-sectional area of the matrix in the X_1X_2 -plane/ X_1X_3 -plane, $\phi^m = 0$ corresponds to undamaged matrix, and $\phi^m = 1$ to the totally damaged matrix. Assuming that the composite is under a uniform average transverse normal stress σ_{22}^c , the balance of forces requires that $\sigma_{22}^c A = \sigma_{22}^m A (1 - \phi^m) = \sigma_{22}^f A$. Following the MoM approach, see e.g. [33], we get the following equation for the transverse modulus, E_2^c :

$$\frac{1}{E_2^c} = \frac{V^f}{E_2^f} + \frac{V^m}{E_2^m (1 - \phi^m)}. \quad (16)$$

Under in-plane shear, a high stress concentration develops at the fiber/matrix interface that can cause shear failure in the matrix and/or fiber/matrix debonding [32]. We

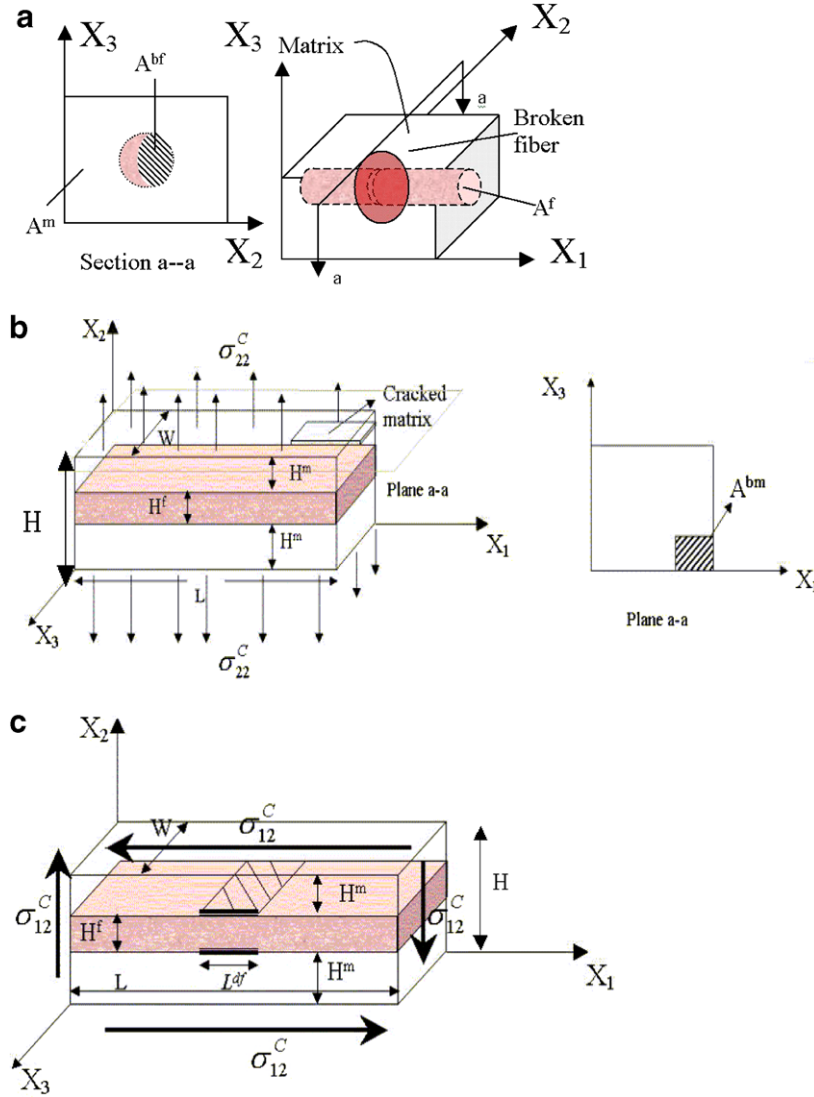


Fig. 1. Composite RVE with (a) broken fiber, (b) cracked matrix, (c) debonded fiber/matrix.

assume that the damage parameter corresponding to the fiber/matrix debonding equals the length, L^{df} , of the fiber that is separated from the matrix material (e.g., see Fig. 1c) divided by the total length of the fiber. That is, $L^{df} = \phi^d L^f$, where L^f is the length of the fiber, $\phi^d = 0$ for the undamaged fiber/matrix bond, and $\phi^d = 1$ for the totally damaged fiber/matrix interface. The effective shear modulus in the X_1X_2 -plane is obtained in a manner similar to the transverse modulus as

$$\frac{1}{G_{12}^C} = \frac{V^f}{G_{12}^f(1 - \phi^d)} + \frac{V^m}{G_{12}^m}. \quad (17)$$

In order to find the effective shear modulus in the X_2X_3 -plane, we assume that the shear forces applied on the X_1X_3 - and the X_1X_2 -planes are uniform. Since the fiber is embedded in the matrix, and the applied force is perpendicular to the debonded length of the fiber, it is postulated that all of the applied force is transmitted to the matrix and the

fiber, and no slippage occurs; $\sigma_{23}^C = \sigma_{23}^m = \sigma_{23}^f$. Therefore, the effective shear modulus in the X_2X_3 -plane is independent of the debonding damage variable.

2.2.3. Damage variables

We postulate that

$$\phi^f = \phi^f(Y^f), \quad \phi^m = \phi^m(Y^m), \quad \phi^d = \phi^d(Y^d) \quad (18)$$

are materially objective functions, and the functional dependence is determined from test data. It is reasonable to assume that the damage at a material point does not increase while the material there is unloading as indicated by a decrease in a suitable scalar measure of stresses and/or strains. Here we assume that in the material principal axes, ϕ^f , ϕ^m , and ϕ^d depend, respectively, on ε_{11} , ε_{22} , and ε_{12} . Furthermore, we presume that a material point is unloading if $d|\varepsilon_{11}|$, $d|\varepsilon_{22}|$, and/or $d|\varepsilon_{12}|$ there is negative. Thus, for unloading from the state of deformation with strains ε_{11}^{\max} , ε_{22}^{\max} and ε_{12}^{\max} ,

$$\begin{aligned} d\phi^f &= 0 \quad \text{if either } d|\varepsilon_{11}| < 0 \text{ or } |\varepsilon_{11}| < |\varepsilon_{11}^{\max}|, \\ d\phi^m &= 0 \quad \text{if either } d|\varepsilon_{22}| < 0 \text{ or } |\varepsilon_{22}| < |\varepsilon_{22}^{\max}|, \\ d\phi^d &= 0 \quad \text{if either } d|\varepsilon_{12}| < 0 \text{ or } |\varepsilon_{12}| < |\varepsilon_{12}^{\max}|. \end{aligned} \quad (19)$$

These relations imply that the evolution of a damage variable is being treated in a way analogous to that of incremental plastic strains for an elastoplastic material. Furthermore, during unloading from, and reloading to the state of deformation corresponding to strains ε_{11}^{\max} , ε_{22}^{\max} and ε_{12}^{\max} , elastic constants are kept fixed at their values for the state of deformation represented by ε_{11}^{\max} , ε_{22}^{\max} and ε_{12}^{\max} .

2.2.4. Failure criteria

It is assumed that the failure due to fiber breakage, matrix cracking, and fiber/matrix debonding occurs when Y^f , Y^m , and Y^d reach their critical values Y_{crit}^f , Y_{crit}^m , and Y_{crit}^d , respectively. Values for Y_{crit}^f , Y_{crit}^m , and Y_{crit}^d depend upon materials of the fiber and the matrix, sizing of fibers, and possibly on the fabrication process; these are to be determined from the experimental data.

In order to simulate delamination between adjoining layers, cracks are allowed to propagate in the interface between them, and they are assumed to be perfectly bonded until a damage surface, defined by

$$D_d = \left(\frac{\sigma_{33}}{[\sigma_{33}]} \right)^2 + \left(\frac{\sigma_{13}}{[\sigma_{13}]} \right)^2 + \left(\frac{\sigma_{23}}{[\sigma_{23}]} \right)^2 = 1, \quad (\sigma_{33} \geq 0), \quad (20)$$

is reached. Here $[x]$ denotes the ultimate value of the quantity x . The failure envelope (20) depends on the transverse normal, and the transverse shear stresses at the interface between two adjoining layers. However, when $\sigma_{33} < 0$, the failure envelope (20) is modified to

$$D_d = \left(\frac{\sigma_{13}}{[\sigma_{13}]} \right)^2 + \left(\frac{\sigma_{23}}{[\sigma_{23}]} \right)^2 = 1, \quad (\sigma_{33} < 0), \quad (21)$$

and the two layers are allowed to slide relative to each other.

2.2.5. Values of material parameters

The composite studied here is AS4/PEEK with $V^f = 0.6$. Materials of the fiber, and the matrix are assumed to be isotropic; values of their parameters taken from Kyriakides et al. [36] are given in Table 1. The procedure for deriving expressions for the damage variables in terms of the conju-

Table 1
Values of material parameters of the fiber and the matrix^a

	Matrix (PEEK)	Carbon fiber (AS4)
Poisson's ratio	0.356	0.263
Young's modulus (GPa)	6.14	214
Shear modulus (GPa)	2.264	84.7
Mass density (g/cm ³)	1.44	1.78

^a The matrix and the fiber are assumed to be isotropic.

gate forces from experimental stress–strain curves, also taken from Kyriakides et al. [36] is described below.

The experimental stress–strain curve for AS4/PEEK deformed in simple tension is exhibited in Fig. 2a; stress–strain curves for transverse tension, and off-axis tests were also used to derive values of elastic constants but are not shown here. Kyriakides et al. [36] reported that the material failed at the last value of the strain plotted in Fig. 2. We assume that during uniaxial loading along the fiber direction, all stress components except σ_{11} identically vanish. The longitudinal modulus of the composite, E_1 , can thus be computed from the axial stress–axial strain curve.

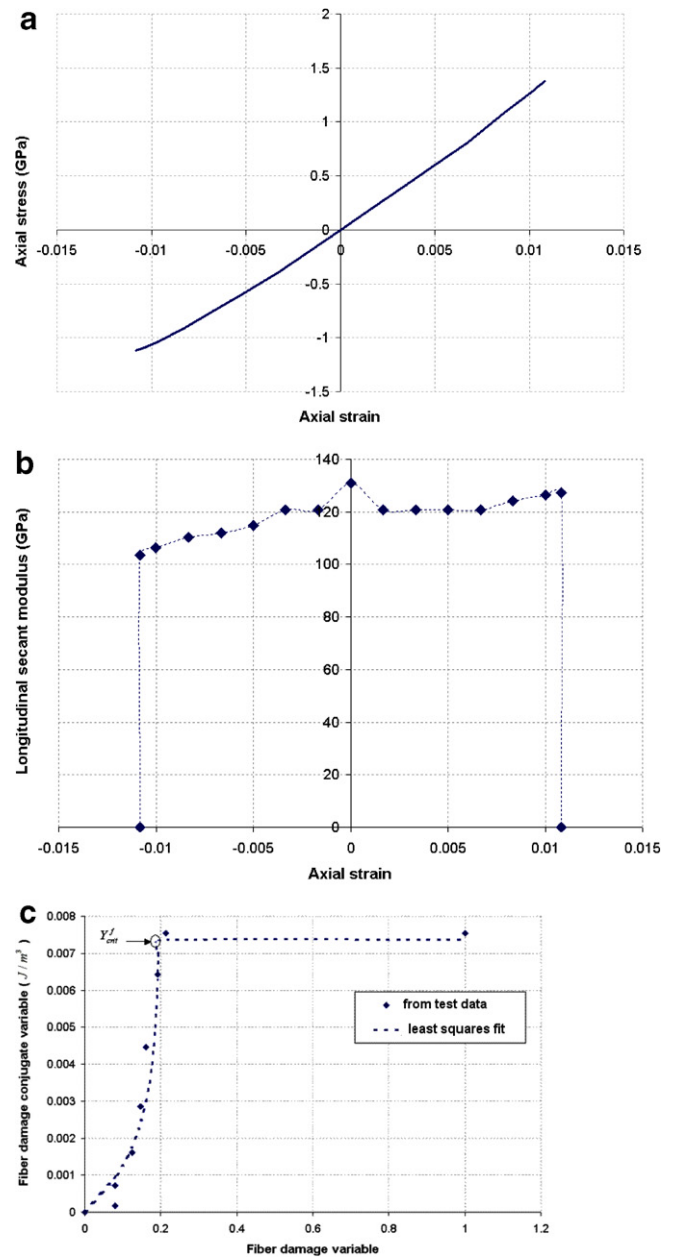


Fig. 2. (a) Experimental uniaxial stress–strain response of APC-2/AS4 composite lamina loaded in the fiber direction, (b) longitudinal secant modulus of the composite versus axial strain, (c) fiber damage conjugate variable versus fiber damage variable for uniaxial compression.

The axial stress versus the axial strain curve in uniaxial tension is nearly linear but that in uniaxial compression is nonlinear. Using values of material parameters listed in Table 1, Eq. (15) that relates the composite longitudinal modulus E_1 to that of the fiber and the matrix, the volume fractions of constituents, and assuming no damage (i.e., $\phi^f = 0$) at $\varepsilon_{11} = 0$, we get composite's longitudinal modulus $E_1 = 130.86$ GPa. It is higher than the 120.65 GPa computed from the slope of the stress–strain curve of Fig. 2a at $\varepsilon_{11} = 0$. Possible sources of this discrepancy are that $\phi^f \neq 0$ at $\varepsilon_{11} = 0$, and one or more of the assumptions made to derive Eq. (15) is invalid. We note that a fabrication process usually introduces defects, voids and/or residual stresses that can not be easily relieved. Here we assume that $\phi^f = 0$ initially, and upon loading the longitudinal modulus drops from 130.86 GPa more or less instantaneously to 120.65 GPa. However, for computational purposes, the latter value of the longitudinal modulus is assigned to an axial strain of 0.002. Fig. 2b shows the longitudinal secant modulus, E_1 , ($=\sigma_{11}/\varepsilon_{11}$) as a function of the axial strain ε_{11} ; it is computed from the axial stress versus the axial strain curve of Fig. 2a. It is not clear why the composite exhibits stiffening behavior in tension beyond an axial strain of 0.007 till an axial strain of 0.011 when it fails. At failure, the secant modulus is assumed to drop to zero within an infinitesimal increment in the axial strain. The decrease in the secant modulus in compression with increasing axial compressive strain is possibly due to the microbuckling of fibers. Magnitudes of the axial strain at failure in uniaxial tension, and in uniaxial compression are nearly the same. Similar procedure is adopted to arrive at the transverse secant modulus variation with the magnitude of the transverse axial strain, and of composite's transverse modulus with shear strain.

Solving Eq. (15) for ϕ^f , Eq. (16) for ϕ^m , and Eq. (17) for ϕ^d , we get

$$\phi^f = 1 - ((E_1 - E_1^m V^m)/E_1^f V^f), \quad (22)$$

$$\phi^m = 1 - (V^m E_2 E_2^f / E_2^m (E_2^f - E_2 V^f)), \quad (23)$$

$$\phi^d = 1 - (V^f G_{12} G_{12}^m / G_{12}^f (G_{12}^m - G_{12} V^m)). \quad (24)$$

In Eqs. (22)–(24), E_1 , E_2 , and G_{12} vary with the corresponding strain component. The expression (14)₂ for the conjugate force $Y^{(i)}$ simplifies to

$$Y^{(q)} = -\frac{1}{2} \frac{\partial \sigma_{ij}}{\partial \phi^{(q)}} \varepsilon_{ij}, \quad q = m, f, d. \quad (25)$$

For uniaxial loading in the fiber direction, only $\sigma_{11} \neq 0$, and Eq. (25) reduces to

$$Y^f = -\frac{1}{2} \frac{\partial \sigma_{11}}{\partial \phi^f} \varepsilon_{11} = -\frac{1}{2} \frac{\partial E_1}{\partial \phi^f} \varepsilon_{11}^2 = \frac{1}{2} E_1^f V^f \varepsilon_{11}^2, \\ Y^m = 0, \quad Y^d = 0. \quad (26)$$

Eq. (26) states that the variable conjugate to the fiber breakage parameter equals the strain energy density of the fiber multiplied by its volume fraction, and the fiber/matrix interaction affects Y^f only through the normal strain

along the fiber. Note that units of Y^f are the same as that of energy density, i.e., J/m³ which can also be written as Pascals.

For a given value of ε_{11} , we compute Y^f from Eq. (26), read E_1 from the curve plotted in Fig. 2b, and then find ϕ^f from Eq. (22). Values so obtained are depicted in Fig. 2c as filled diamonds. The curve, obtained by the least squares fit to these data points till Y^f reaches its critical value Y_{crit}^f , is given by

$$\phi^f = A_f (1 - e^{(-B_f Y^f)}), \quad (27)$$

where values of constants A_f and B_f , that are different in tension and compression, are listed in Table 2.

Following the procedure analogous to that adopted to deduce Eqs. (26) and (27), we obtain the following from uniaxial tests in the transverse direction, and the off-axis loading in the $X_1 X_2$ -plane.

$$Y^m = -\frac{1}{2} \frac{\partial \sigma_{22}}{\partial \phi^m} \varepsilon_{22} = -\frac{1}{2} \frac{\partial E_2}{\partial \phi^m} (\varepsilon_{22})^2 = \frac{1}{2} \frac{E_2^m E_2^f V^f}{(E_2^m V^f (1 - \phi^m) - E_2^f V^m)^2} (\varepsilon_{22})^2, \quad (28)$$

$$\phi^m = \left(\frac{A_m B_m + C_m (Y^m)^{D_m}}{B_m + (Y^m)^{D_m}} \right), \quad (29)$$

$$Y^d = -\frac{1}{2} \frac{\partial \sigma_{12}}{\partial \phi^d} 2\varepsilon_{12} = -\frac{\partial G_{12}}{\partial \phi^d} (\varepsilon_{12})^2 = \frac{(G_{12}^f)^2 G_{12}^m V^f}{(G_{12}^m V^f - G_{12}^f (1 - \phi^d) V^m)^2} (\varepsilon_{12})^2, \quad (30)$$

$$\phi^d = \left(\frac{A_d B_d + C_d (Y^d)^{D_d}}{B_d + (Y^d)^{D_d}} \right). \quad (31)$$

We note that there is no simple energetic interpretation for conjugate forces Y^m and Y^d . Values of constants A_m , B_m , C_m , D_m , A_d , B_d , C_d , D_d , found in a way similar to that of ascertaining A_f and B_f are listed in Table 2. For a general loading, and/or when fibers are not aligned with the

Table 2
Values of constants in Eqs. (27), (29), (31), (20) and (21)

Damage properties		Tension	Compression
Fiber breakage	A_f	1.931 GPa	0.197 GPa
	B_f	1.931497	558
	Y_{crit}^f	0.0075 GPa	0.007535 GPa
Matrix cracking	A_m	1.356×10^{-10} GPa	0.01207 GPa
	B_m	0.00193	174
	C_m	0.37239 GPa	241 GPa
	D_m	0.43665	0.195
	Y_{crit}^m	0.0005 GPa	0.011 GPa
Fiber/matrix debonding	A_d	0.1437 GPa	
	B_d	0.00762	
	C_d	1.0022 GPa	
	D_d	0.37714	
	Y_{crit}^d	5.48×10^{-2} GPa	
Interfacial strength ^a	$[\sigma_{33}]$	0.078 GPa	
	$[\sigma_{13}]$	0.157 GPa	
	$[\sigma_{23}]$	0.157 GPa	

^a Values for the ultimate interfacial strength were obtained from a composite data base site <http://composite.about.com/library/data/blc-as4apc2-1.htm>.

loading axis, we first analyze the problem in the global coordinate system, and then compute the normal strain along the fiber. The sign of ε_{11} dictates which values of A_f , B_f and Y_{crit}^f to use in Eq. (27). We follow a similar procedure for selecting appropriate values of A_m , B_m , C_m , D_m and Y_{crit}^m in Eq. (29), and of A_d , B_d , C_d , D_d and Y_{crit}^d in Eq. (31). In Table 2, Y_{crit}^f , Y_{crit}^m , and Y_{crit}^d equal values of conjugate variables corresponding, respectively, to ϕ^f , ϕ^m and ϕ^d equaling 1.0, i.e., failure of the material point due to fiber breakage, matrix cracking, and fiber/matrix debonding. We have also listed, in Table 2, values for ultimate strengths $[\sigma_{33}]$, $[\sigma_{13}]$ and $[\sigma_{23}]$; these appear in Eqs. (20) and (21), and determine when, and where delamination occurs.

2.2.6. Strain rate effect

Eqs. (27), (29) and (31) when solved for conjugate variables in terms of damage parameters give

$$Y^f = \frac{-\log\left(\frac{A_f - \phi^f}{A_f}\right)}{B_f}, \quad (32)$$

$$Y^m = \left(\frac{B_m(-A_m + \phi^m)}{C_m - \phi^m}\right)^{1/D_m}, \quad (33)$$

$$Y^d = \left(\frac{B_d(-A_d + \phi^d)}{C_d - \phi^d}\right)^{1/D_d}. \quad (34)$$

We now postulate the following functional dependence of conjugate damage variables Y^m and Y^d upon $\dot{\varepsilon}_{22}$ and $\dot{\gamma}_{12}$ respectively:

$$Y^m = \left(\frac{B_m\left(-A_m + \phi^m\left(1 - s^m \log_{10}\left(\frac{\dot{\varepsilon}_{22}}{\dot{\varepsilon}_{22}^0}\right)\right)\right)}{C_m - \phi^m\left(1 - s^m \log_{10}\left(\frac{\dot{\varepsilon}_{22}}{\dot{\varepsilon}_{22}^0}\right)\right)}\right)^{1/D_m}, \quad (35)$$

$$Y^d = \left(\frac{B_d\left(-A_d + \phi^d\left(1 - s^d \log_{10}\left(\frac{\dot{\gamma}_{12}}{\dot{\gamma}_{12}^0}\right)\right)\right)}{C_d - \phi^d\left(1 - s^d \log_{10}\left(\frac{\dot{\gamma}_{12}}{\dot{\gamma}_{12}^0}\right)\right)}\right)^{1/D_d}. \quad (36)$$

Here $\dot{\varepsilon}_{22}^0$ and $\dot{\gamma}_{12}^0$ represent, respectively, values of the reference transverse and the reference shear strain rates. Eq. (32) is assumed to be independent of strain rate; it is based on the observation that the experimental stress–strain curve for AS4/PEEK in longitudinal tension and compression is essentially insensitive to the axial strain rate.

We now discuss the determination of material constants s^m and s^d appearing in Eqs. (35) and (36) from the transverse compression, and the in-plane shear experimental stress–strain curves for AS4/PEEK at various strain rates [2]. We note that for the transverse compression tests, $1.6 \times 10^{-5} \leq \dot{\varepsilon}_{22} \leq 1.6 \times 10^0/s$, and for the in-plane shear tests, $1 \times 10^{-5} \leq 2\dot{\varepsilon}_{12} \leq 1 \times 10^{-1}/s$. For each strain rate, we follow the procedure described in Section 2.2.5, and obtain curves plotted in Fig. 3 that depict the variation of Y^m versus ϕ^m .

By comparing Eqs. (33) and (35), we conclude that Eq. (35) is obtained from Eq. (33) when ϕ^m in Eq. (33) is

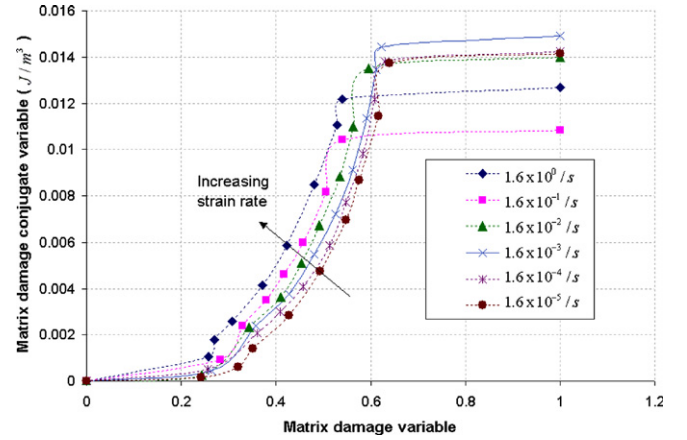


Fig. 3. Matrix damage conjugate variable versus matrix damage parameter at different values of the strain rate $\dot{\varepsilon}_{22}$.

replaced by $\phi^m\left(1 - s^m \log_{10}\left(\frac{\dot{\varepsilon}_{22}}{\dot{\varepsilon}_{22}^0}\right)\right)$. Similarly, Eq. (36) can be gotten from Eq. (34) when ϕ^d in Eq. (34) is replaced by $\phi^d\left(1 - s^d \log_{10}\left(\frac{\dot{\gamma}_{12}}{\dot{\gamma}_{12}^0}\right)\right)$. The value of the material parameter s^m is found by plotting in Fig. 4 $\left(1 - \frac{\phi^m}{\phi^m|_{\dot{\varepsilon}_{22}^0}}\right)$ versus $\log_{10}\left(\frac{\dot{\varepsilon}_{22}}{\dot{\varepsilon}_{22}^0}\right)$ at $Y^m = 0.006$, and setting $\dot{\varepsilon}_{22}^0 = 1.6 \times 10^{-5}/s$. It is found that the least squares fit to the data points is a straight line passing through the origin. The slope, 0.0361, of this line equals s^m . A similar procedure is adopted to find the value 0.0013 of the material constant s^d ; in this case the data is plotted for $Y^d = 0.03$, and the reference shear strain rate, $\dot{\gamma}_{12}^0$, equals $1 \times 10^{-5}/s$.

Here we have taken the damage variables ϕ^m and ϕ^d to depend upon strain rates that is inconsistent with the assumption made to derive Eq. (7). A possibility is to hypothesize that the Helmholtz free energy has additive decomposition into two parts – one that is independent of strain rates, and the other depends upon strain rates. One can then postulate constitutive relation (14). In either case, one needs a constitutive relation for S^{ne} . For the work

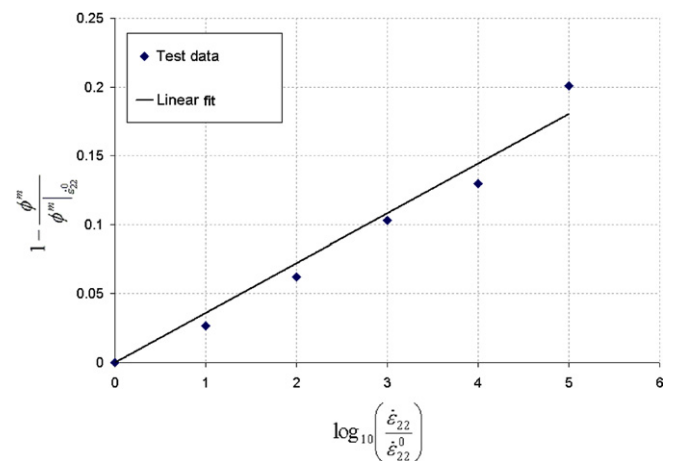


Fig. 4. Variation of $\left(1 - \frac{\phi^m}{\phi^m|_{\dot{\varepsilon}_{22}^0}}\right)$ with $\log_{10}\left(\frac{\dot{\varepsilon}_{22}}{\dot{\varepsilon}_{22}^0}\right)$ at $Y^m = 0.006$ for $\dot{\varepsilon}_{22}^0 = 1.6 \times 10^{-5}/s$.

presented here, the constitutive relation for \mathbf{S} is obtained from that for \mathbf{S}^e with ϕ^m and ϕ^d replaced, respectively, by $\phi^m \left(1 - s^m \log_{10} \left(\frac{\dot{\epsilon}_{22}}{\dot{\epsilon}_0}\right)\right)$ and $\phi^d \left(1 - s^d \log_{10} \left(\frac{\dot{\gamma}_{12}}{\dot{\gamma}_0}\right)\right)$, and $\mathbf{S}^{ne} = \mathbf{S} - \mathbf{S}^e$. One may interpret constitutive relations presented here as being physical relations since they are derived from experimental data.

The material constant, Y_{crit}^i ($i = f, m, d$), was assumed to be independent of the strain rate because failure strains in Vogler and Kyriakides [2] do not exhibit any clear dependency upon the strain rate. Similarly, for a lack of test data, the interfacial strengths, $[\sigma_{33}]$, $[\sigma_{13}]$, and $[\sigma_{23}]$, of the composite are assumed to be strain rate independent.

2.3. Mathematical model

2.3.1. Governing equations

Substitutions from Eq. (14) into Eq. (2) give the following nonlinear field equation for the determination of the displacement \mathbf{u} :

$$\rho_R \ddot{\mathbf{u}}_i = [(\delta_{ix} + u_{i,x})(C_{\alpha\beta\gamma\delta} E_{\gamma\delta})]_{,\beta} + \rho_R b_i. \quad (37)$$

Since the AS4/PEEK composite fails at small values of strains, effects of geometric nonlinearities on the computed solution will be negligible except in buckling problems where the present formulation will enable one to compute the post-buckled response; buckling problems have not been studied here. Also, all stress tensors have essentially the same values.

2.3.2. Initial and boundary conditions

In the total Lagrangian description of motion, the independent variables are \mathbf{X} and t , and the dependent variables are \mathbf{x} or \mathbf{u} since knowing \mathbf{x} , the present mass density can be computed from Eq. (1). Let Ω be the region occupied by the body in the reference configuration at time $t = 0$. A general form of boundary and initial conditions is

$$\begin{aligned} x_i(\mathbf{X}, t) &= \bar{x}_i(\mathbf{X}, t), \quad \mathbf{X} \in \partial_X \Omega, \quad t \in (0, \tilde{T}), \\ T_{ix}(\mathbf{X}, t) N_x(\mathbf{X}) &= f_i(\mathbf{X}, t), \quad \mathbf{X} \in \partial_f \Omega, \quad t \in (0, \tilde{T}), \\ x_i(\mathbf{X}, 0) &= X_\alpha \delta_{i\alpha}, \\ \dot{x}_i(\mathbf{X}, 0) &= v_i^0(\mathbf{X}). \end{aligned} \quad (38)$$

Here $\partial_X \Omega$, and $\partial_f \Omega$ are parts of the boundary $\partial \Omega$ of Ω where final positions (or equivalently, displacements), and surface tractions are prescribed, respectively, as \mathbf{x} , and \mathbf{f} . Note that $\partial_X \Omega$, and $\partial_f \Omega$ need not be disjoint since linearly independent components of displacements, and surface tractions may be specified at the same point on $\partial \Omega$. Initial values of internal variables representing the fiber breakage, fiber/matrix debonding, and matrix cracking are taken to be zeros.

3. Numerical solution

A weak form of Eq. (37) is derived by using the Galerkin approximation; e.g. see Hughes [37]. It reduces nonlinear partial differential Eq. (37) to nonlinear ordinary differen-

tial equations, which are integrated with respect to time t by using the subroutine LSODE (Livermore Solver for Ordinary Differential Equations) that adaptively adjusts the time step size, and computes the solution within the prescribed accuracy.

A 3-dimensional (3-D) finite element (FE) code based on the afore-stated problem formulation has been developed in Fortran. Degrees of freedom at each node are three components of displacement, and three components of velocity since LSODE integrates first order ODEs. The code employs 8-node brick elements, and various domain integrals involving integration on an element Ω_e that appear in the weak formulation of the problem are evaluated by using the $2 \times 2 \times 2$ Gauss quadrature rule. During the time integration of the coupled ODEs with the subroutine LSODE, absolute and relative error tolerances were each set equal to 1×10^{-9} , and MF was assigned the value 10. The parameter MF determines the integration method in LSODE, and MF = 10 implies using the Adam–Moulton method. After having found nodal displacements, values of conjugate variables, and damage parameters (or internal variables) ϕ^f , ϕ^m and ϕ^d at each integration point are determined; these are used to update elastic constants for computing results at the next time step.

3.1. Simulation of material failure

When, at a material (or an integration) point, an internal variable ϕ^f , ϕ^m , and/or ϕ^d equals 1.0, or the corresponding conjugate variable Y^f , Y^m , and Y^d equals its critical value, the material there is taken to have failed due to fiber breakage, matrix cracking, and/or fiber matrix debonding, respectively. Even if the material at all eight integration points within an element has failed, that element is not removed from the analysis. Once all elastic constants at the eight integration points in an element have been reduced to zero, all stress components in that element will subsequently be zero, and for all practical purposes that element will represent a hole or a void except that it has kinetic energy.

In order to simulate either sliding or crack initiation and propagation due to delamination, we assume that when the stress state at a node N has reached the failure envelope (20) or (21), an additional node N^* coincident with N but not connected to it is added there. The nodal connectivity of elements sharing the node N is modified in the sense that one or more of these elements is now connected to the newly added node N^* rather than the node N . However, no new element is created in this process. We note that delamination may ensue simultaneously at several nodes. If subsequent deformations of the body move nodes N and N^* apart and create new surfaces, then these surfaces are taken to be traction free. The non-interpenetration of nodes N and N^* into the material is avoided by connecting them with a 1-D two-node spring element that is weak in tension but stiff in compression. The constitutive relation for the stiff spring is taken to be

$$F = kz_n,$$

where

$$k = \begin{cases} 0, & z_n/z_0 \geq 0, \\ E_3^l \left[1 + (\eta E_3 - 1) \left(\frac{z_n}{z_0} \right)^2 \right], & -1 \leq z_n/z_0 < 0, \\ \eta E_3^l, & z_n/z_0 < -1. \end{cases} \quad (39)$$

Here F is the normal force between nodes N and N^* , E_3 Young’s modulus of the composite in the X_3 -direction, z_n the relative displacement between nodes N and N^* normal to the interface, l a characteristic length, and η a constant. This technique of modeling material failure is similar to that used in [38,46]. Another possibility is to employ cohesive elements; e.g., see [47].

3.2. Verification of the computer code

The code was verified by analyzing a 1-D wave propagation problem, and comparing computed results with those obtained from another code developed by Batra and Love [38] that had been thoroughly tested. Also, for a material with no evolving damage, the code has been verified by using the method of “fictitious” body forces. That is, for a given body, and analytical expressions for the displacement field \mathbf{u} , the field of fictitious body force \mathbf{b} is derived from Eq. (2). Also, initial and boundary conditions corresponding to the presumed field are deduced. These side conditions, and field \mathbf{b} are used as input into the computer code to find the corresponding displacement \mathbf{u} . If the so computed values of \mathbf{u} match with those obtained from their presumed analytical solutions, then the computer code has been verified. A similar procedure was used by Batra and Liang [39]; e.g., see the material following Eq. (30) of their paper. The validity of the code and of the model for problems in which damage evolves is established below.

3.3. Validity of the proposed model

The proposed model is validated by comparing computed results for different test configurations with the corresponding experimental data. The AS4/PEEK composite has 60% volume fraction of fibers. Values of material parameters for the 0° undamaged lamina are listed in Table 3. Twenty-six test configurations, including two involving

uniaxial loading, unloading, and reloading, have been simulated.

Unless specified otherwise, the body is taken to be initially at rest, and stress-free.

3.3.1. Uniaxial tensile/compressive or in-plane shear loads

Five test configurations employed by Kyriakides et al. [36] and summarized in Table 4 were numerically simulated. The specimen dimensions, the prescribed speed at the two opposite end faces, and the number of elements employed in the FE mesh are listed in Table 3; in each case the average axial, transverse or shear strain rate equals $10^{-5}/s$. Also, each one of the four plies in the composite had fibers oriented along the X_1 -axis; thus it can be viewed as a single lamina made of a homogeneous transversely isotropic material with X_1 -axis as the axis of transverse isotropy.

Computed stress–strain curves for these five cases are compared in Fig. 5a–c with the experimental ones [36]. In each case, computed results agree well with the test data as should have been expected since data from these tests were used to deduce values of material parameters. We note that the maximum strain at any point is about 4%; thus the geometric nonlinearity has a negligible effect on computed deformations. In order to economize on the CPU time, mass densities of the fiber, and the matrix were reduced to 0.1% of their actual values. It increases the wave speed thereby making transients propagate faster in the specimen.

Fig. 6a–c depicts the evolution of the three damage variables with the axial strain which may be interpreted as non-dimensional time since the nominal axial strain rate is kept constant at $10^{-5}/s$. For longitudinal and transverse loading, the only active damage modes are the fiber breakage, and the matrix cracking respectively. Under longitudinal loading, the fiber breakage damage variable begins to evolve at essentially a constant rate at an axial strain of 0.001 till an axial strain of 0.007 is reached. It subsequently evolves very slowly until the axial strain equals 0.011 when it rapidly increases to its maximum value of 1.0. The time evolution of the matrix cracking damage variable can be divided into three distinct parts, each with a different rate of evolution, between transverse strains of 0 and 0.001, 0.001 and 0.00825, and between 0.00825 and the final strain where it equals its maximum value of 1.0. Under shear loads both fiber/matrix debonding, and matrix cracking damage variables begin to evolve simultaneously but at

Table 3
Values of material parameters of the undamaged 0° AS4/PEEK lamina with $V^f = 0.6$

Material parameter	Value
ν_{12}	0.3
E_1 (GPa)	130.86
E_2 (GPa)	14.7
G_{12} (GPa)	5.44
G_{23} (GPa)	5.44
ρ (g/cm ³)	1.64

Table 4
Parameters for the five uniaxial loading tests simulated

Loading	Specimen size (mm)	\bar{v} (mm/min)	FE mesh
Longitudinal tension	152.4 × 12.7 × 1.27	0.045	120-12-4
Longitudinal compression	31.8 × 9.53 × 9.53	−0.01	40-12-12
Transverse tension	83.8 × 15.8 × 2.54	0.025	30-8-4
Transverse compression	76.2 × 6.73 × 6.73	−0.02	40-8-8
Shear	196 × 10.26 × 2.54	0.006	80-8-4

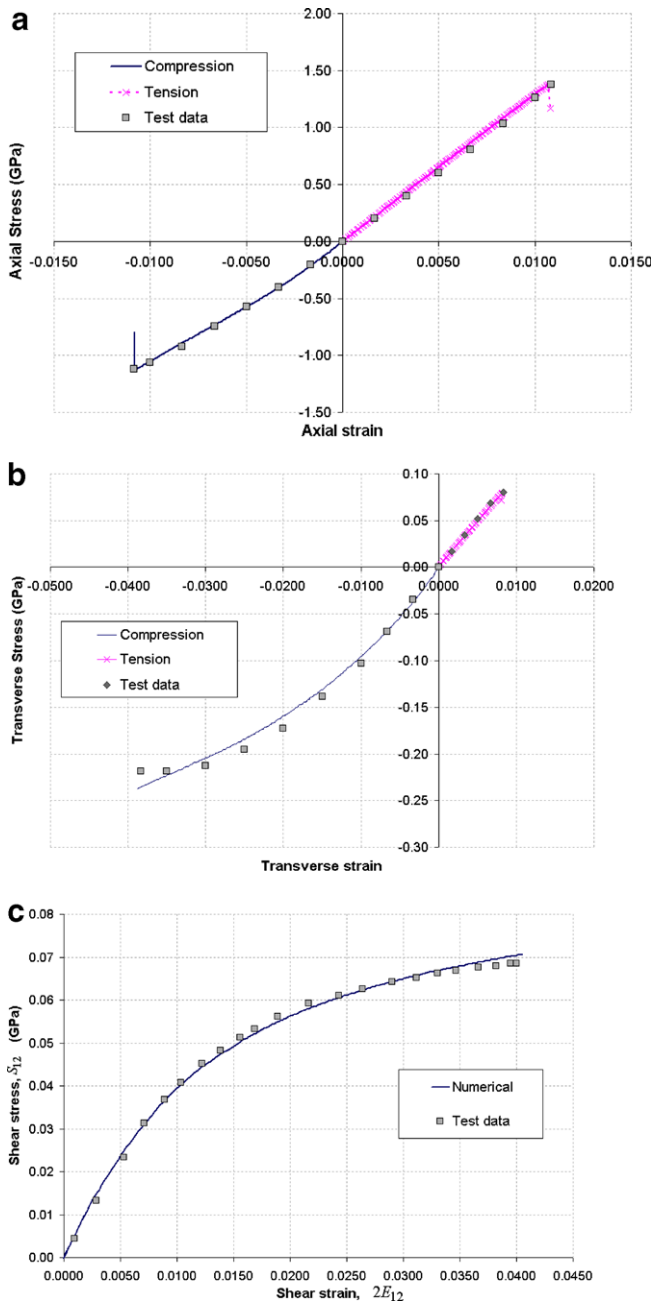


Fig. 5. Comparison of the computed (a) axial stress–axial strain, (b) transverse axial stress versus transverse axial strain, and (c) shear stress–shear strain curves at the specimen centroid with experimental data of Kyriakides et al. [36].

quite different rates. The rate of evolution of the matrix cracking damage variable increases with an increase in the axial strain till the axial strain equals 0.006; subsequently its rate of evolution slows down. Whereas at low values of the axial strain, the matrix cracking damage variable is less than the fiber/matrix debonding variable, the reverse occurs for axial strains exceeding 0.0035. The computed failure modes agree qualitatively with those observed experimentally by Diao et al. [40] who tested $[0]_{16}$ laminate in longitudinal, and transverse tension. They found that the fiber breakage failure mode was dominant in laminates

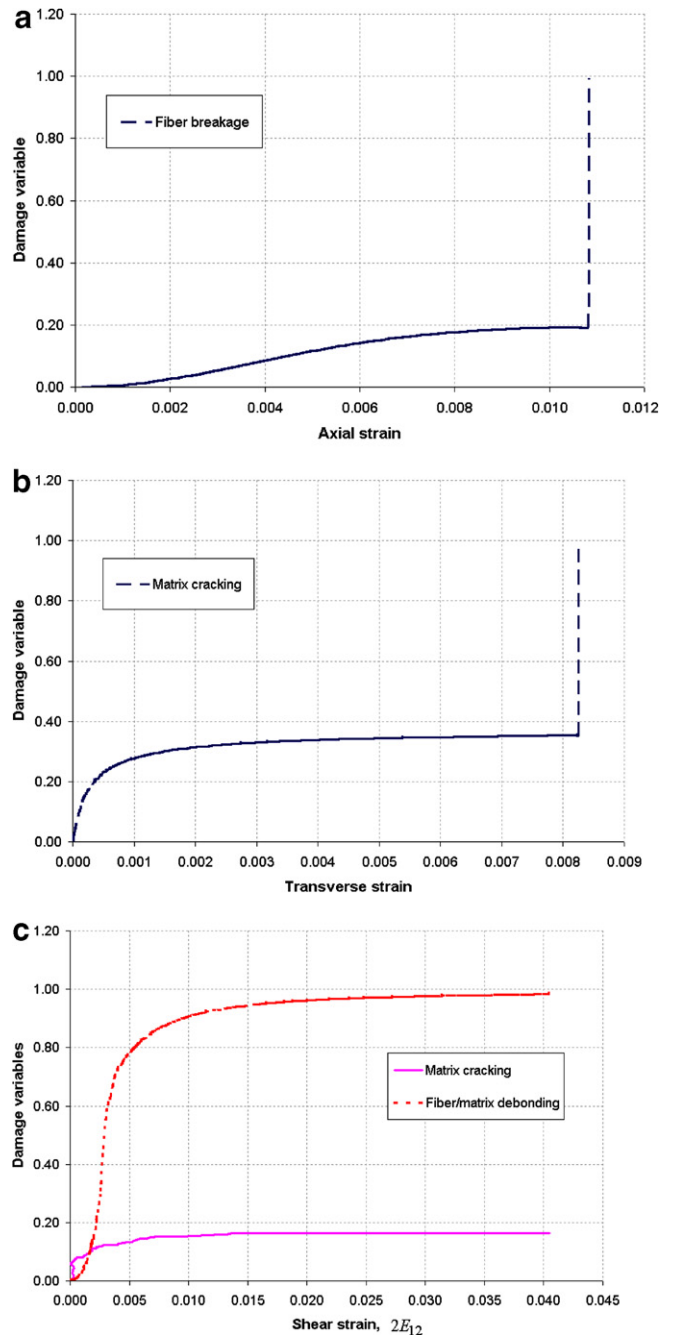


Fig. 6. Evolution with the axial strain of (a) fiber breakage, (b) matrix cracking, and (c) fiber/matrix debonding damage and matrix cracking variables for longitudinal tensile, transverse tensile, and shear loading, respectively, of AS4/PEEK composite.

loaded longitudinally, and the matrix cracking mode in laminates pulled in the transverse direction. For all the three loading cases, computed deformations are nearly homogeneous. The material fails at an axial strain of 1.09% for the longitudinal tensile loading, at a transverse strain of 0.825% for the transverse tensile loading, and at an axial strain of about 4% for the shear loading.

In Fig. 7a and b we have compared computed axial stress versus axial strain curves with the corresponding

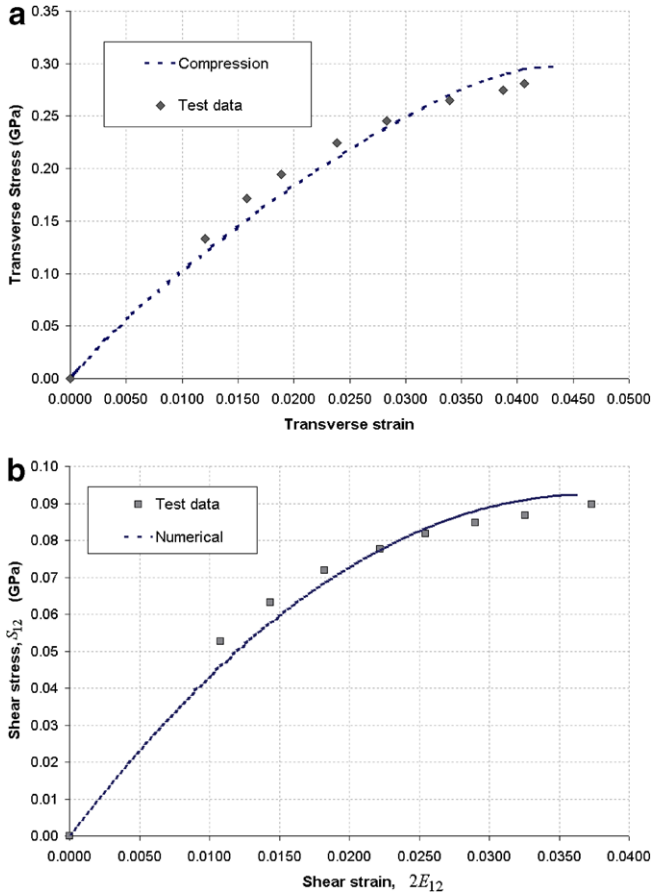


Fig. 7. Comparison of computed (a) transverse compressive stress versus transverse compressive strain, and (b) shear stress versus shear strain for AS4/PEEK composite deformed at a strain rate of 0.1/s with the experimental data of Vogler and Kyriakides [2].

experimental ones [36] for specimens deformed either in transverse compression or in simple shear at a strain rate of 0.1/s which is four orders of magnitude higher than that for test results reported in Fig. 6a–c. The 76.2 mm × 6.73 mm × 6.73 mm specimen deformed in transverse compression was divided into a uniform 40 × 8 × 8 FE mesh, and the other 196 mm × 10.26 mm × 2.54 mm specimen into 80 × 8 × 4 FE mesh. In each case, computed and experimental stress versus strain curves are very close to each other.

3.3.2. Off-axis loads

Four-ply composites of over-all dimensions 216 mm × 15.9 mm × 2.54 mm, divided into a uniform 84 × 6 × 4 FE mesh, were loaded along the global X_1 -axis by pulling the opposite end faces at an equal and opposite axial speed of 0.065 mm/min or equivalently at an average axial strain rate of $\sim 10^{-5}$ /s. For five configurations simulated, identically oriented fibers in each ply made an angle of 15°, 30°, 45°, 60° or 75° counterclockwise with the X_1 -axis. Weeks and Sun [41], and Jen and Lee [42] have experimentally tested these specimens. Note that results of these experiments are not used to find values of material param-

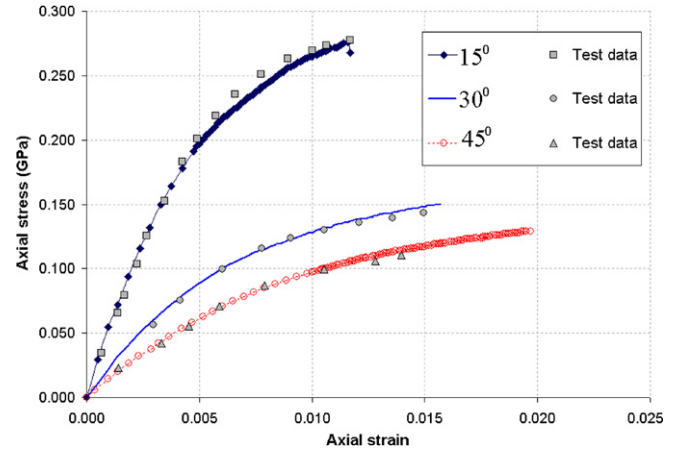


Fig. 8. Comparison of the computed axial stress versus axial strain curve of AS4/PEEK with experimental data of Weeks and Sun [41] for three fiber orientations.

eters for the AS4/PEEK composite. Thus the comparison of computed results with experimental observations of Refs. [41,42] provides a good test for the proposed model.

Computed axial stress–axial strain curves for fiber orientation angles of 15°, 30° and 45° are compared with the corresponding experimental ones in Fig. 8; it is evident that the two sets of curves match very well. The dependence of the ultimate axial tensile stress, and the axial failure strain upon the fiber orientation angle is shown in Fig. 9a and b respectively. Whereas the ultimate tensile strength has the maximum value for the 0° fiber orientation, the axial failure strain has the maximum value for a fiber orientation of 45°. The ultimate tensile strength drops off very rapidly as the fiber orientation angle is increased from 0° to 15°; however, the further decreases in the tensile strength with subsequent increases in the fiber orientation angle by 15° are quite small.

We did not conduct numerical experiments for fiber orientations between 0° and 15°, and therefore cannot decipher whether the drop in the tensile strength is asymptotic or linear.

For the uniaxial loading, stresses at a point for the 15°, and the 75° fiber orientations are quite different. Thus plots of the ultimate axial tensile stress versus the fiber orientation angle, θ , need not be symmetric about $\theta = 45^\circ$; the same holds for the plot of the axial strain at failure versus the fiber orientation angle. Jen and Lee [42] did not plot the axial stress versus the axial strain curve; thus our computed curves for $\theta = 60^\circ$ and 75° laminate cannot be compared with the corresponding experimental ones. However, their tabulated values 115 MPa and 96 MPa, respectively, for the ultimate strength of 60° and 75° laminate agree well with our computed values of 103 MPa and 83 MPa. They found the ultimate tensile strength of a [45]₁₆ composite to be 151.0 MPa; our results plotted in Fig. 9a give a value of 129 MPa. They stated that the failure surface was parallel to the fibers, and was roughed by matrix cracks,

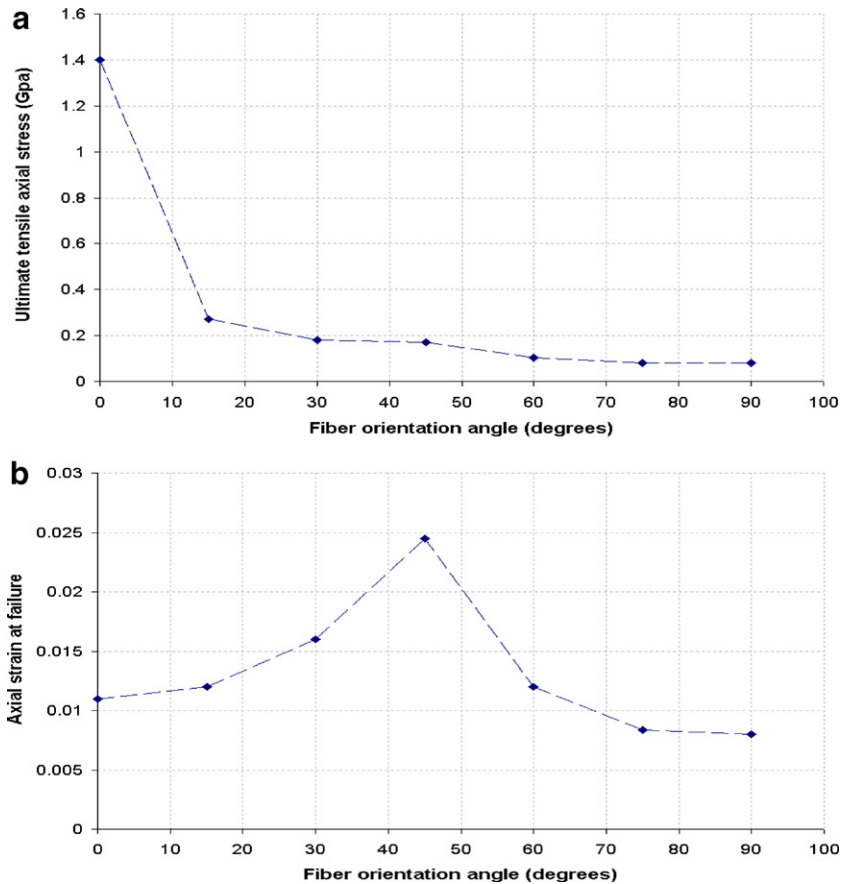


Fig. 9. Dependence upon the fiber orientation angle of (a) the ultimate axial tensile strength, and (b) the axial strain at failure, for unidirectional quasistatic loading of a composite.

implying thereby that the fiber/matrix debonding failure mode was dominant.

3.3.3. Balanced plies

For the sixth configuration, fiber orientation in plies 1 (the bottom-most), 2, 3, and 4 (the top-most) equaled 30° , -30° , -30° and 30° respectively; this lay-up is referred

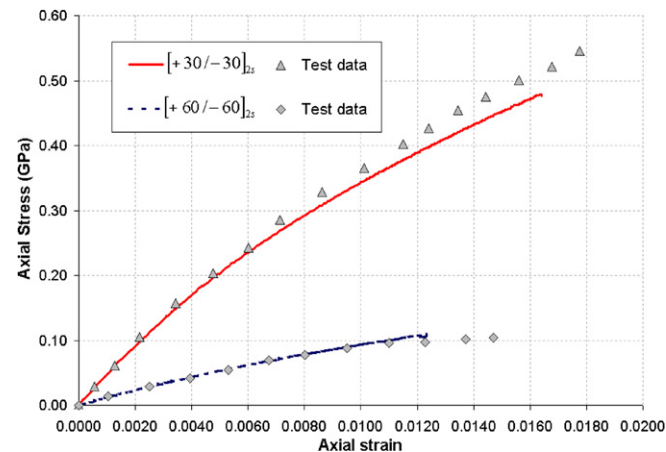


Fig. 10. Comparison of the computed axial stress versus axial strain curve of AS4/PEEK with experimental data of Weeks and Sun [41] for 2 balanced $[+30^\circ/-30^\circ]_{2s}$ plies at strain rate of 0.01/s.

to as balanced plies, $[+30^\circ/-30^\circ]_{2s}$. A 216 mm \times 15.9 mm \times 2.54 mm specimen, divided into a uniform $84 \times 6 \times 4$ FE mesh, was loaded along the global X_1 -axis by pulling the opposite end faces at an equal and opposite axial speed of 65 mm/min, or equivalently at an average axial strain rate of $\sim 10^{-2}$ /s. A seventh configuration with same dimensions but fiber orientation of $[+60^\circ/-60^\circ]_{2s}$ was loaded along the global X_1 -axis by pulling the opposite end faces at an equal and opposite axial speed of 65 mm/min, or equivalently at an average axial strain rate of $\sim 10^{-2}$ /s. Results of those two configurations are compared in Fig. 10 with the experimental data from Weeks and Sun [41]. It is evident that computed results are close to those obtained experimentally with a maximum difference of 4% in the ultimate stress, and of 20% in the failure strain.

3.3.4. Strain-rate effects

Weeks and Sun [41] tested 8 mm \times 8 mm \times 8 mm 32-ply $[30^\circ/-30^\circ]_{16s}$, and $[60^\circ/-60^\circ]_{16s}$ composites in a split Hopkinson pressure bar at nominal strain rates of 300/s, and 1000/s respectively. We simulate these tests by assuming that deformations are symmetrical about the midsurface, and pressure loads on the left and the right faces of the specimen can be replaced by the prescribed axial velocity that increases from 0 to $4\dot{\epsilon}$ in $0.1 \mu\text{s}$ where $\dot{\epsilon}$ equals the nominal axial strain rate. The specimen was discretized with a

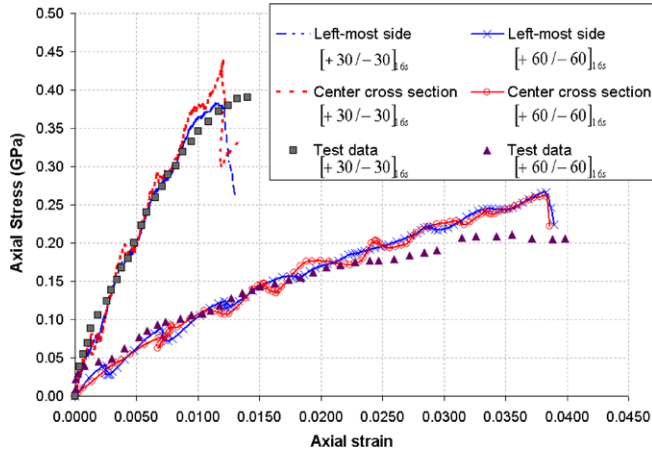


Fig. 11. Comparison of the computed axial stress versus axial strain curve of AS4/PEEK with experimental data of Weeks and Sun [41] for [+30°/-30°]16s laminate at strain rate of 300/s, and [+60°/-60°]16s laminate at strain rate of 1000/s.

uniform $16 \times 16 \times 16$ FE mesh. Computed axial stress versus axial strain curves for the two strain rates are compared with the corresponding experimental ones [41] in Fig. 11. It is clear that the fiber orientation angle affects significantly the axial stress induced in the specimen for a given value of the axial strain. For specimens with identical layout of fibers the axial stress at a given value of the axial strain will be higher in the specimen deformed at an axial strain rate of $10^3/s$ than that in the specimen deformed at an axial strain rate of $300/s$. However, here the reverse occurs because of differences in the fiber layout. Whereas the $[30^\circ/-30^\circ]_{16s}$ laminate deformed at an axial strain rate of $300/s$ failed at $t = 19.7 \mu s$, the $[60^\circ/-60^\circ]_{16s}$ laminate deformed at an axial strain rate of $1000/s$ failed at $t = 21.8 \mu s$. The axial strain at failure for each specimen matches well that observed experimentally.

This simulation and that reported below in Section 3.3.5 provide a severe test of the proposed model since material constants were found from tests of Kyriakides et al. [36] on a single lamina deformed at strain rates of $10^{-5}/s$ to $10^{-1}/s$, and here computed results have been compared for a 16-ply laminate deformed at axial strain rates of $3 \times 10^2/s$ and $1 \times 10^3/s$. Furthermore, plies in the two laminates have different fiber orientations.

3.3.5. Low velocity impact loads

Schoeppner and Abrate [43] have experimentally determined damage induced in a laminated composite impacted by a 2.54 cm diameter hemispherical hardened steel ball dropped from a known height. The load applied by the steel ball is numerically simulated by applying a pressure field distributed over a circular cross-section of radius R ;

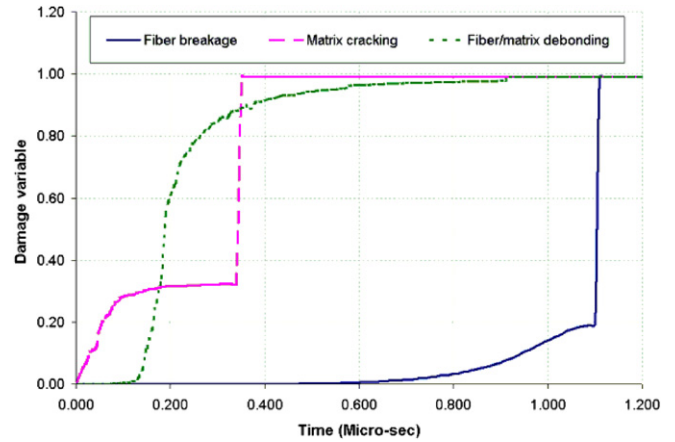


Fig. 12a. Time histories of evolution of the three damage variables, ϕ^f , ϕ^m and ϕ^d , at the centroid of 1.27 mm thick specimen.

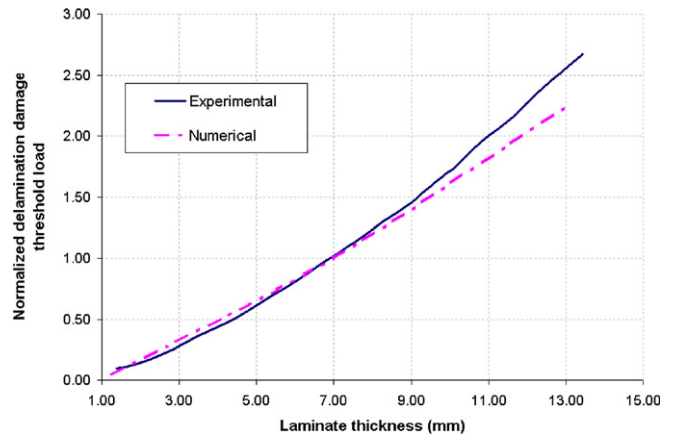


Fig. 12b. Comparison of the dependence upon the laminate thickness of the numerically computed and the experimentally observed [43] normalized damage threshold load.

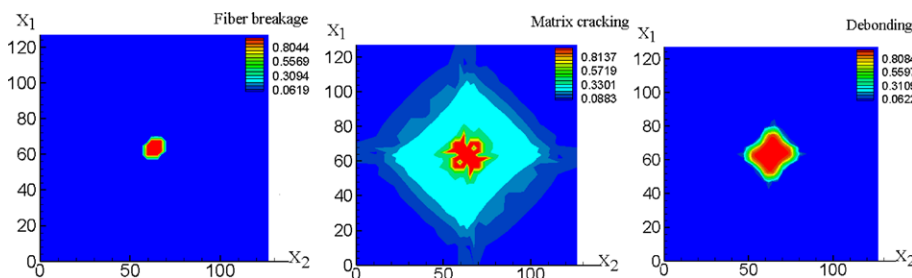


Fig. 12c. Fringe plots of the damage variables at time = 1.48 μs .

the value of R depends upon the applied load, and elastic constants of the laminate and of the steel. The value of R is found from the following Hertz's [44] relations:

$$R^3 = \frac{3}{4} \pi a P (\zeta_{\text{steel-sphere}} + \zeta_{\text{composite}}),$$

$$P' = \frac{3P}{2\pi R^2} \sqrt{1 - \frac{x^2}{R^2} - \frac{y^2}{R^2}}, \quad \zeta = (\lambda + 2\mu)/4\pi\mu(\lambda + \mu),$$
(40)

where λ and μ are Lamé's constants, P' is the pressure acting at a point, a is the radius of the sphere, and P equals the total applied load. Values of λ and μ for the composite were calculated using material properties at each integration point on the contact surface, and the following relations:

$$\lambda = \frac{0.3E_3}{(1+0.3)(1-2(0.3))}, \quad \mu = \frac{E_3}{2(1+0.3)},$$
(41)

where E_3 is the modulus of the composite in the X_3 -direction, and Poisson's ratio is taken to be 0.3. P is assumed to increase linearly with time at the rate of 0.75 kN/ μ s. Fiber orientations in the 9 layers starting from the top layer equaled 45, -45 , 0, 0, 90, -45 , 45°. The thickness of the laminate in the five simulations equaled 1.27 mm, 4 mm, 7 mm, 11 mm, and 13 mm. For each thickness, the laminate was divided into $20 \times 20 \times 9$ 8-node brick elements with a finer mesh in the impacted area.

For a 1.27 mm thick laminate, time histories of evolution of the three damage variables, ϕ^f , ϕ^m and ϕ^d , at the laminate centroid are depicted in Fig. 12a. The Damage Threshold Load (DTL) is the load at which damage increases quickly, and the load drops rapidly. We took it to be the load when the three damage variables reach 1 at the specimen centroid (Fig. 12b). As can be seen from results plotted in Fig. 12a, for the 1.27 mm thick laminate, this occurred at time = 1.48 μ s, giving DTL = 1.11 kN. The DTL for laminates of different thicknesses has been normalized by the DTL for the 7-mm thick laminate since for it the experimental and numerical values equaled 12.5 kN. As shown in Fig. 14b, the numerically computed DTL matches well with that found experimentally. Fringe plots of ϕ^f , ϕ^m and ϕ^d at $t = 1.48 \mu$ s are exhibited in Fig. 12c.

3.3.6. Loading, unloading and reloading

Instead of applying a constant velocity on the opposite edges of the 75° 1 mm \times 0.1 mm \times 0.1 mm laminate, we prescribed either an alternating velocity, or an oscillating tensile-compressive surface traction to opposite edges to simulate loading, unloading and reloading; schematics of these problems are shown in Figs. 13a and 14a, respectively. For axial velocity prescribed at opposite faces, Fig. 13b and c depict, respectively, the axial stress–axial strain, and time histories of evolution of the three damage variables at the center of the left edge (i.e., the point $X_1 = 0$, $X_2 = 0.05$, $X_3 = 0.05$) of the specimen. The stress–strain curve during unloading of the specimen differs from that

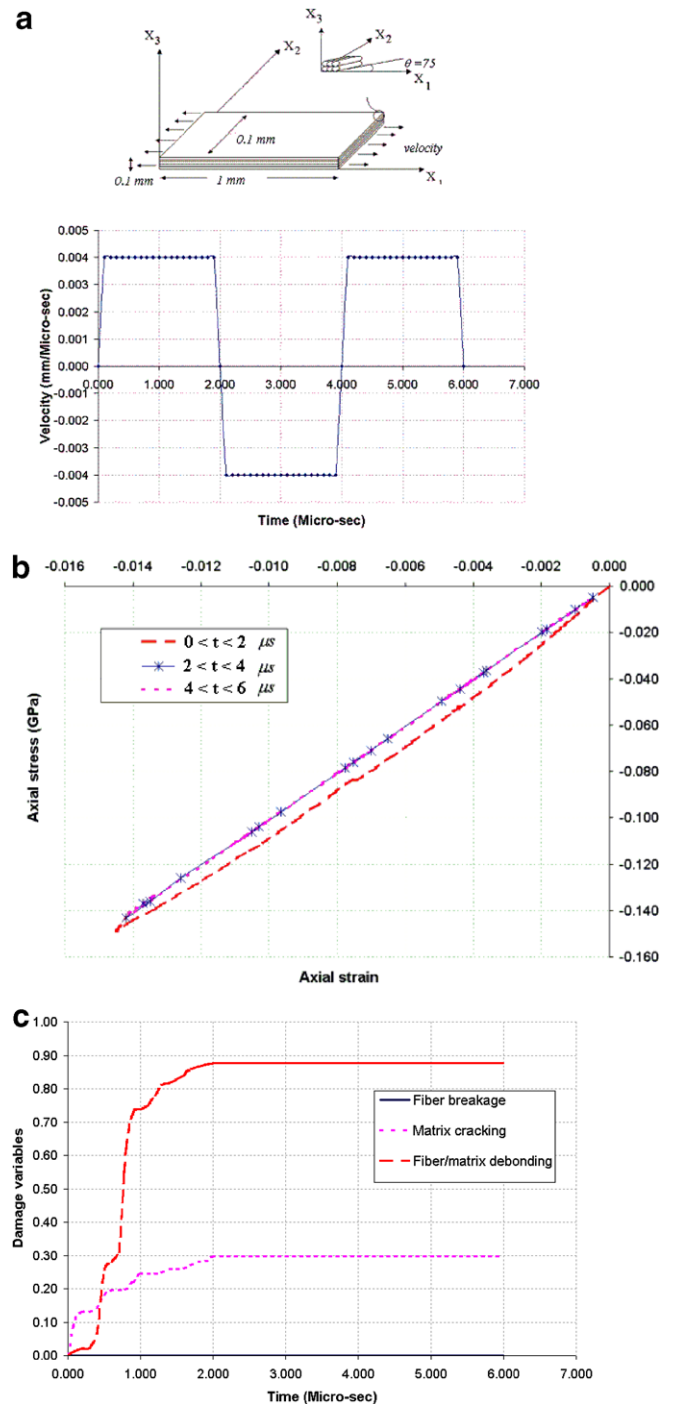


Fig. 13. (a) Schematic sketch of the problem studied, and time history of the axial velocity prescribed at the opposite edges; (b) axial stress–axial strain at the point $X_1 = 0$, $X_2 = 0.05$ mm, and $X_3 = 0.05$ mm; (c) time histories of evolution of the three damage variables, ϕ^f , ϕ^m and ϕ^d , at the centroid of 1.27 mm thick specimen.

during initial loading due to the difference in the elastic moduli caused by the damage developed during loading. As can be seen from the plots of Fig. 13c, there is virtually no fiber breakage, and for $t > 0.5 \mu$ s, the debonding damage variable has a considerably higher value than the matrix cracking damage variable. Furthermore, for $t > 2 \mu$ s, these damage variables have constant values since

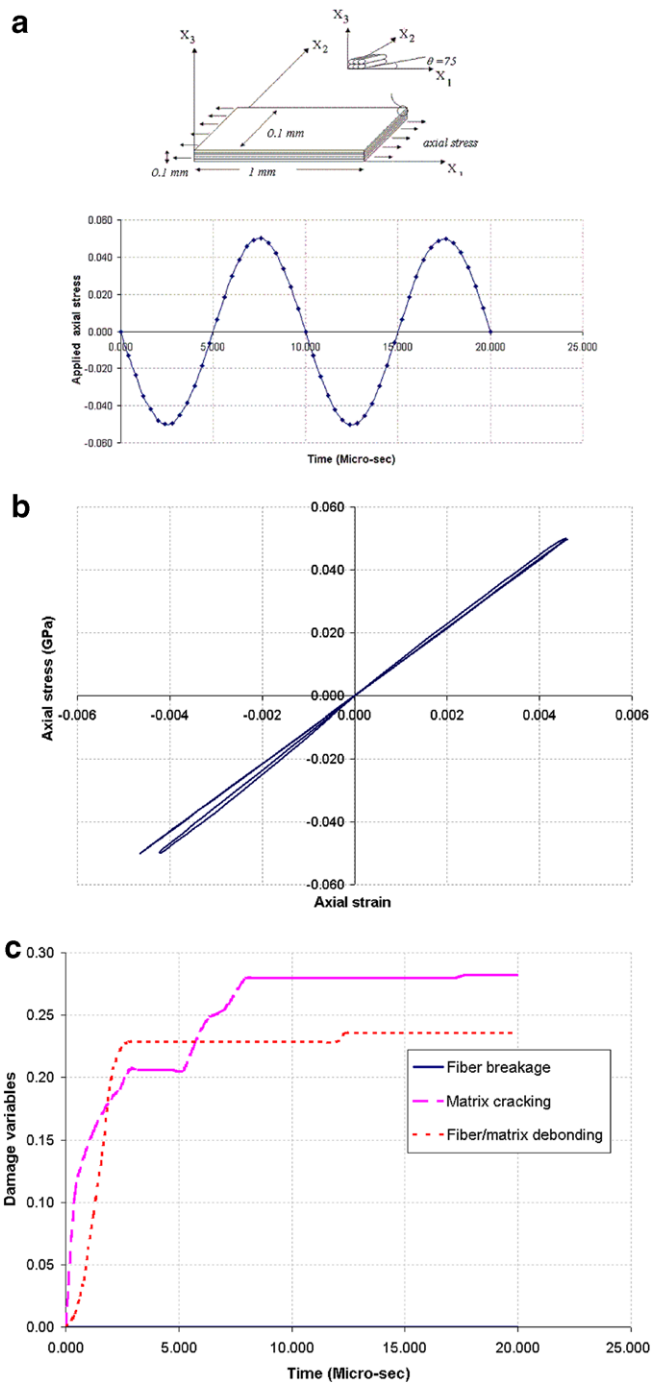


Fig. 14. (a) Schematic sketch of the problem studied, and time history of the axial surface traction (GPa) prescribed at the opposite edges; (b) axial stress–axial strain at the point $X_1 = 0$, $X_2 = 0.05$ mm and $X_3 = 0.05$ mm; (c) time histories of evolution of the three damage variables at $X_1 = 0$, $X_2 = 0.05$ mm and $X_3 = 0.05$ mm.

then either the material is unloading or strains induced in the material are below their previously reached limiting values for the additional damage to develop. Thus during repeated loading and unloading under prescribed axial velocity of constant amplitude, there will be no additional damage developed, and the proposed model predicts a rather unrealistic infinite life of the laminate.

Fig. 14b and c depict, respectively, the axial stress–axial strain, and time histories of evolution of the three damage variables at the center of the left edge (i.e. $X_1 = 0$, $X_2 = 0.05$ and $X_3 = 0.05$) of the laminate when equal and opposite axial tractions are applied on its opposite edges. There is essentially no fiber breakage induced, and the dominant damage modes are debonding and matrix cracking. The damage variables remain unchanged during unloading of the material point but evolve during reloading because of the higher strains induced in the damaged material. Thus, the proposed model can be used to predict fatigue life of the specimen for cyclic traction loading.

4. Conclusions

We have developed a model for a laminated composite that can predict well damage induced in it under different loading conditions. Experimental stress strain curves during axial, transverse, and off-axis loading are used to find values of material parameters. These parameters are then used to compute results for configurations and loadings totally different from the ones employed to calibrate the model. It is found that the proposed mathematical model can satisfactorily predict failure strains, damage evolved, and other deformation variables under a variety of loadings. The close agreement between computed and experimental results for widely different loadings and geometries suggests that the proposed model is robust.

In particular, equations governing finite deformations of an anisotropic composite, the evolution of damage, and those describing the degradation of material parameters with damage are given. The present value of a damage variable representing fiber breakage, fiber/matrix debonding, or matrix cracking at a material point is assumed to depend upon the state of deformation at that material point. The delamination failure is considered by allowing the two adjoining laminas to either locally separate from or slide over each other whenever the failure criterion at a point on the interface has been satisfied. The elastic response of the material is modeled by assuming it to be neo-Hookean, and the strain-rate response by assuming that the evolution of damage variables also depends upon the strain rate. A finite element code for analyzing three-dimensional transient deformations employing 8-node brick elements has been developed, and used to analyze various initial-boundary-value problems for the AS4/PEEK laminated composite. Computed results have been found to compare well with corresponding experimental results available in the literature. The framework developed herein has been employed by Batra and Hassan [48,49] to analyze the blast response of composite structures under different loading scenarios.

Acknowledgements

This work was partially supported by the ONR grants N00014-01-98-3000 and N00014-1-06-0567 to Virginia

Polytechnic Institute and State University (VPI&SU) with Dr. Y.D.S. Rajapakse as the program manager. Views expressed herein are those of authors, and neither of funding agencies nor of VPI&SU.

References

- [1] Vinçon I, Allix O, Sigety P, Auvray M. Compressive performance of carbon fibres: experiment and analysis. *Compos Sci Technol* 1998;58(10):1649–58.
- [2] Vogler T, Kyriakides S. Inelastic behavior of an AS4/PEEK composite under combined transverse compression and shear, Part I: Experiments. *Int J Plasticity* 1999;15(8):783–806.
- [3] Stout M, Koss D, Liu C, Idasetima J. Damage development in carbon/epoxy laminates under quasi-static and dynamic loading. *Compos Sci Technol* 1999;59(16):2339–50.
- [4] Gilbert M, Hobbs B, Molyneux T. The performance of unreinforced masonry walls subjected to low-velocity impacts: experiments. *Int J Impact Eng* 2002;27(3):231–51.
- [5] Steeves C, Fleck N. Collapse mechanisms of sandwich beams with composite faces and a foam core loaded in three-point bending. Part II: Experimental investigation and numerical modeling. *Int J Mech Sci* 2004;46(4):585–608.
- [6] Matzenmiller A, Lubliner J, Taylor R. A constitutive model for anisotropic damage in fiber composites. *Mech Mater* 1995;20(2):125–52.
- [7] Zhu Y, Cescotto S. A fully coupled elasto-visco-plastic damage theory for anisotropic materials. *Int J Solids Struct* 1995;32(11):1607–41.
- [8] Voyiadjis G, Deliktas B. A coupled anisotropic damage model for the inelastic response of composite materials. *Comput Methods Appl Mech Eng* 2000;183(3–4):159–99.
- [9] Zhu C, Sun C. A viscoplasticity model for characterizing loading and unloading behavior of polymeric composites. In: *Time dependent and nonlinear effects in polymers and composites*. ASTM; 2000.
- [10] Espinosa H, Dwivedi S, Lu H. Modeling impact induced delamination of woven fiber reinforced composites with contact/cohesive laws. *Comput Methods Appl Mech Eng* 2000;183(3–4):259–90.
- [11] Williams K, Vaziri R. Application of a damage mechanics model for predicting the impact response of composite materials. *Comput Struct* 2000;79:997–1011.
- [12] Tang X, Jiang C, Zheng J. Anisotropic elastic constitutive relations for damaged materials by application of irreversible thermodynamics. *Theor Appl Fract Mech* 2002;38(3):211–20.
- [13] Maa R, Cheng J. A CDM-based failure model for predicting strength of notched composite laminates. *Compos Part B: Eng* 2002;33(6):479–89.
- [14] Kachanov L. On the creep rupture time. *Izv Akad Nauk SSSR* 1958;8:26–31.
- [15] Rabotnov Y. On the equations of state for creep. *Progress in applied mechanics*. Prager Anniversary vol. New York: Macmillan; 1963.
- [16] Coleman B, Noll W. On the thermostatics of Continuous Media. *Arch Ration Mech Anal* 1959;4:97–128.
- [17] Talreja R. A continuum mechanics characterization of damage in composite materials. *Proc Royal Soc London* 1985;399:195–216.
- [18] Ladevèze P. A damage computational method for composite structures. *Comput Struct* 1992;44(1–2):79–87.
- [19] Barberis U, Hassim A, Ravera C, Vanderborck G. Impact-induced damage analysis tool for laminated composites. *Advances in Composite Materials & Structures VII*. Boston: WIT Press; 2000.
- [20] Krajcinovic D, Fonseka GU. The continuous damage theory of brittle materials. Part I: General theory. *J Appl Mech* 1981;48:809–15.
- [21] Carol I, Rizzi E, Willam K. On the formulation of anisotropic elastic degradation. I. Theory based on a pseudo-logarithmic damage tensor rate. *Int J Solids Struct* 1965;38(4):491–518.
- [22] Carol I, Rizzi E, William K. On the formulation of isotropic and anisotropic damage. *Comput Model Concrete Struct* 1998:183–92. Austria.
- [23] Chaboche JL, Lesne PM, Maire JF. Continuum damage mechanics. Anisotropy and damage deactivation for brittle materials like concrete and ceramic composites. *Int J Damage Mech* 1995;4:5–22.
- [24] Lemaitre J, Desmorat R, Sauzay M. Anisotropic damage law of evolution. *Eur J Mech – A/Solids* 2000;19(2):187–208.
- [25] Voyiadjis G Z, Guelzim Z. A coupled incremental damage and plasticity theory for metal matrix composites. *J Mech Behavior Mater* 1996;6:193–219.
- [26] Voyiadjis GZ, Park T. The kinematics of damage for finite-strain elasto-plastic solids. *Int J Eng Sci* 1999;37(7):803–30.
- [27] Krajcinovic D. Damage mechanics. *Mech Mater* 1989;8:117–97.
- [28] Simo J, Ju J. Strain- and stress-based continuum damage models—I. Formulation. *Int J Solids Struct* 1987;23(7):821–40.
- [29] Ortiz M. A constitutive theory for the inelastic behavior of concrete. *Mech Mater* 1985;4(1):67–93.
- [30] Batra RC. Comparison of results from four linear constitutive relations in isotropic finite elasticity. *Int J Nonlinear Mech* 2001;36:421–32.
- [31] Christensen R. *Mechanics of composite materials: recent advances*. New York: Pergamon Press; 1982.
- [32] Daniel I, Ishai O. *Engineering mechanics of composite materials*. New York: Oxford University Press; 1994.
- [33] Herakovich C. *Mechanics of fibrous composites*. New York: John Wiley & Sons; 1998.
- [34] Jones R. *Mechanics of composite materials*. USA: Taylor & Francis; 1999.
- [35] Agarwal B, Broutman L. *Analysis and performance of fiber composites*. New York: Wiley; 1990.
- [36] Kyriakides S, Arseculeratne R, Perry E, Liechti K. On the compressive failure of fiber reinforced composites. *Int J Solids Struct* 1995;32(6–7):689–738.
- [37] Hughes TJR. *The finite element method*. NJ: Prentice Hall; 1988.
- [38] Batra RC, Love BM. Crack propagation due to brittle and ductile failures in microporous thermoelastoviscoplastic functionally graded materials. *Eng Fracture Mech* 2005;72:1954–79.
- [39] Batra RC, Liang XQ. Finite dynamic deformations of smart structures. *Comp Mech* 1997;20:427–38.
- [40] Diao X, Ye L, Mai Y. Fatigue behaviour of CF/PEEK composite laminates made from Commingled Prepreg. Part I: Experimental studies. *Compos Part A: Appl Sci Manufactur* 1997;28(8):739–47.
- [41] Weeks CA, Sun CT. Modeling non-linear rate-dependent behavior in fiber-reinforced composites. *Compos Sci Technol* 1998;58(3–4):603–11.
- [42] Jen M, Lee C. Strength and life in thermoplastic composite laminates under static and fatigue loads. Part I: Experimental. *Int J Fatigue* 1998;20(9):605–15.
- [43] Schoeppner G, Abrate S. Delamination threshold loads for low velocity impact on composite laminates. *Compos Part A: Appl Sci Manufactur* 2000;31:903–15.
- [44] Hertz H. *Über Die Berührung Fester Elastischer Körper und Über Die Härte*. Verhdlg. Ver. Bef. Gewerbef. Berlin.1882.
- [45] Batra RC. *Elements of continuum mechanics*. Reston, USA: AIAA; 2005.
- [46] Batra RC, Lear MH. Simulation of brittle and ductile fractures in an impact loaded prenotched plate. *Int J Fracture* 2004;126:179–203.
- [47] Batra RC, Love BM. Cohesive zone modeling of failure and the formation of adiabatic shear bands in particulate composites. Pending publication.
- [48] Batra RC, Hassan NM. Blast resistance of unidirectional fiber reinforced composites. *Compos Part B*, accepted for publication.
- [49] Batra RC, Hassan NM. Response of fiber reinforced composites to underwater explosive loads. *Compos Part B* 2007;38:448–58.